

<https://doi.org/10.1038/s41612-025-01156-z>

Complex gas-particle partitioning of nitro-phenolic compounds: field-based insights and determination of apparent activity coefficient

Check for updates

Yi Chen^{1,2}, Men Xia^{3,4,5}, Penggang Zheng¹, Yumin Li⁶, Zhouxing Zou², Shengrui Tong⁷, Kun Li⁸, Xin Feng¹, Lirong Hui¹, Qi Yuan³, Jinjian Li², Jian Zhen Yu^{1,2}, Shuncheng Lee³, Tao Wang³ & Zhe Wang¹ ✉

Gas–particle partitioning (GPP) of oxygenated semi-volatile organic compounds (SVOCs) is crucial for atmospheric organic aerosol formation, yet large uncertainties persist in its simulation due to challenges in obtaining accurate parameters. This study focuses on nitro–phenolic species (NPs), representative oxygenated SVOCs impacting solar radiative balance and atmospheric chemistry. Concurrent measurements of gaseous and particulate NPs at a subtropical coastal site showed particulate fractions ranging from 8.6% to 53%, which deviated from traditional theoretical estimates by factors of 0.26 to 10^4 . To address these discrepancies, a field-based activity coefficient (ζ) was derived by integrating measured parameters and theoretical considerations. Incorporating ζ into a box model significantly improved simulations for mono–NPs and uncovered a more complex GPP process for di–NPs than previously recognized. The successful application of ζ in a regional model highlights its broader applicability and calls for more quantitative studies for various SVOCs.

Organic aerosols (OA) have become the predominant component of fine particulate matter (PM_{2.5}) in many regions^{1,2}. Despite their recognized importance in air quality, climate change, and human health, accurately simulating their formation in models remains a significant challenge due to gaps in understanding their formation mechanisms and accurate parameterization^{3,4}. Semi-volatile organic compounds (SVOCs) play a crucial role in OA formation through the dynamic gas-particle partitioning (GPP) process. While many attempts have been made to comprehend the GPP of SVOCs, the focus has mainly been on hydrocarbon species such as polycyclic aromatic hydrocarbons (PAHs) and alkanes that are dominated by primary emissions, leaving knowledge gaps regarding oxygenated compounds due to a lack of effective instruments^{5–8}. However, with the mitigation of primary SVOCs, oxygenated SVOCs have become increasingly important, emphasizing the necessity to understand the GPP for those oxygenated compounds.

Nitro–phenolic species (NPs), characterized by the presence of $-\text{NO}_2$ and $-\text{OH}$ substituents attached to a benzene ring, are considered as typical oxygenated SVOCs based on their physicochemical properties and volatility range. Many studies have confirmed their presence in both the gas and particle phases under ambient atmospheric conditions^{9–11}. NPs can originate from primary emissions such as coal combustion, vehicle exhaust, and biomass burning, as well as from secondary formation via oxidation of aromatic precursors^{11–15}. In addition to their phytotoxic effects, NPs are also recognized as key chromophores in brown carbon (BrC), with strong light absorption at wavelengths greater than 360 nm, thereby affecting solar radiative balance and modulating atmospheric oxidation capacity via photolysis^{9,10,16–20}. Therefore, accurate characterization of their GPP is crucial for quantifying their roles in atmospheric chemistry and climate change. However, the current understanding of the GPP of NPs is limited to only

¹Division of Environment and Sustainability, The Hong Kong University of Science and Technology, Hong Kong SAR, China. ²Department of Chemistry, The Hong Kong University of Science and Technology, Hong Kong SAR, China. ³Department of Civil and Environmental Engineering, The Hong Kong Polytechnic University, Hong Kong SAR, China. ⁴Institute for Atmospheric and Earth System Research/Physics, Faculty of Science, University of Helsinki, Helsinki, Finland. ⁵Nanjing–Helsinki Institute in Atmospheric and Earth System Sciences, Nanjing University, Nanjing, China. ⁶Institute for Atmospheric and Climate Science, ETH Zürich, Zürich, Switzerland. ⁷State Key Laboratory for Structural Chemistry of Unstable and Stable Species, Beijing National Laboratory for Molecular Sciences (BNLMS), CAS Research/Education Center for Excellence in Molecular Sciences, Institute of Chemistry, Chinese Academy of Sciences, Beijing, China. ⁸Qingdao Key Laboratory for Prevention and Control of Atmospheric Pollution in Coastal Cities, Environment Research Institute, Shandong University, Qingdao, China.

✉ e-mail: z.wang@ust.hk

variations in species, seasons, and locations^{11,15}. Besides, inconsistencies between the field-derived GPP coefficient (K_{ep}) and the theoretical estimations have been reported for NPs in previous studies^{5,10,21}. For example, the particulate fraction (F_p), defined as the ratio of particulate concentration of one species to its total concentration in both gas and particle phases, for $C_6H_5NO_3$ was underestimated by three orders of magnitude compared to ambient observations¹⁰. These phenomena underscore the urgency of comprehensively investigating the GPP of NPs.

Many theoretical methods have been established to estimate the GPP of SVOCs, among which Pankow's absorption equilibrium theory (Eq. 1) as the foundation of many other theories, is the most used and has been used to estimate the GPP of NPs on aerosols in previous studies^{5,10,21}. As shown in Eq. 1,

$$K_{ep} = \frac{760 \times f_{om} \times R \times T}{10^6 \times P^0 \times MW_{om} \times \zeta} \quad (1)$$

K_{ep} ($m^3/\mu g$) describes the ability of SVOCs to enter the particle phase and is determined by factors such as the fraction of organic matter in the particle phase (f_{om}), temperature (T , K), the average molecular weight of organic matter (MW_{om} , g/mol), activity coefficient (ζ), gas constant (R , $8.2 \times 10^{-5} m^3 atm mol^{-1} K^{-1}$), and the vapor pressure of the subcooled liquid (P^0 , Torr)^{22,23}. In addition to the expression used in Eq. 1, which represents the classical form of the absorption equilibrium theory^{22,23}, alternative formulations are also available (Eq. S2 and S3 in the Supporting Information), applying different standard units for calculating K_{ep} ²⁴. Among these parameters, f_{om} , T , and MW_{om} can be directly measured or estimated, contributing minor uncertainty to K_{ep} estimation. P^0 for most oxygenated SVOCs can only be obtained from theoretical estimation, as has been widely used in previous studies. ζ accounts for the deviation from ideal behavior in a non-ideal mixture of chemical substances, and is influenced by the structure of SVOCs, aerosol composition, and interactions between SVOCs and aerosol components²⁵. Previous studies have emphasized the species-specific nature of ζ in the real atmosphere, yet it is still commonly assumed to be 1 in many modeling efforts, as it is for pure substances, due to the difficulty of

accurately determining activity coefficients in complex aerosol mixtures^{14,26}. Though the estimated K_{ep} with this assumption only differed by one to two orders of magnitude from the measurements for most alkanes and PAHs, the difference could be up to 10^6 times for oxygenated SVOCs, indicating significant uncertainties in the assumption for oxygenated species^{5–8,27–29}. The Universal Quasi-Chemical Functional-group Activity Coefficients (UNIFAC) model was developed to estimate specific ζ values for organics, but challenges in obtaining comprehensive and accurate parameters for the estimation, along with its incomplete consideration of interactions between species, may introduce uncertainties and limit its broader application^{30,31}. While a few studies have investigated the ζ value for several oxygenated SVOCs in laboratory experiments^{30,32,33}, simplified aerosol components may result in different ζ values compared to the real atmosphere^{34,35}. The unknown uncertainty in P^0 estimation and challenges in obtaining ζ prevent us from accurately describing the GPP of oxygenated SVOCs. Recent advancements in instrumentation have enabled the simultaneous measurement of gaseous and particulate oxygenated SVOCs^{8,29}, which motivate the idea of whether an apparent ζ can be derived from the field measurement for oxygenated SVOCs with theoretically estimated P^0 to capture their GPP under real-world conditions.

Here, a field campaign was conducted to concurrently measure gaseous and particulate NPs at a coastal background site in Hong Kong using a Time-of-Flight Chemical Ionization Mass Spectrometry (ToF-CIMS) coupled with a Filter Inlet for Gases and AEROSOLS (FIGAERO). The GPP of NPs was examined and compared with theoretical estimations. The observation-based ζ for each NP was determined and discussed. Benefiting from the high-time-resolution results, the evolutions of F_p of NPs were captured and further investigated by an observation-based box model (OBM) combined with the derived ζ .

Results and Discussion

Characteristics of NPs and comparison to theoretical estimation

A series of homologs of NPs including 14 types of mono-NPs ($C_{6-9}H_xNO_3$, $C_{6-9}H_xNO_4$, $C_{6-8}H_xNO_5$, $C_{7-9}H_xNO_6$) and 6 types of di-NPs

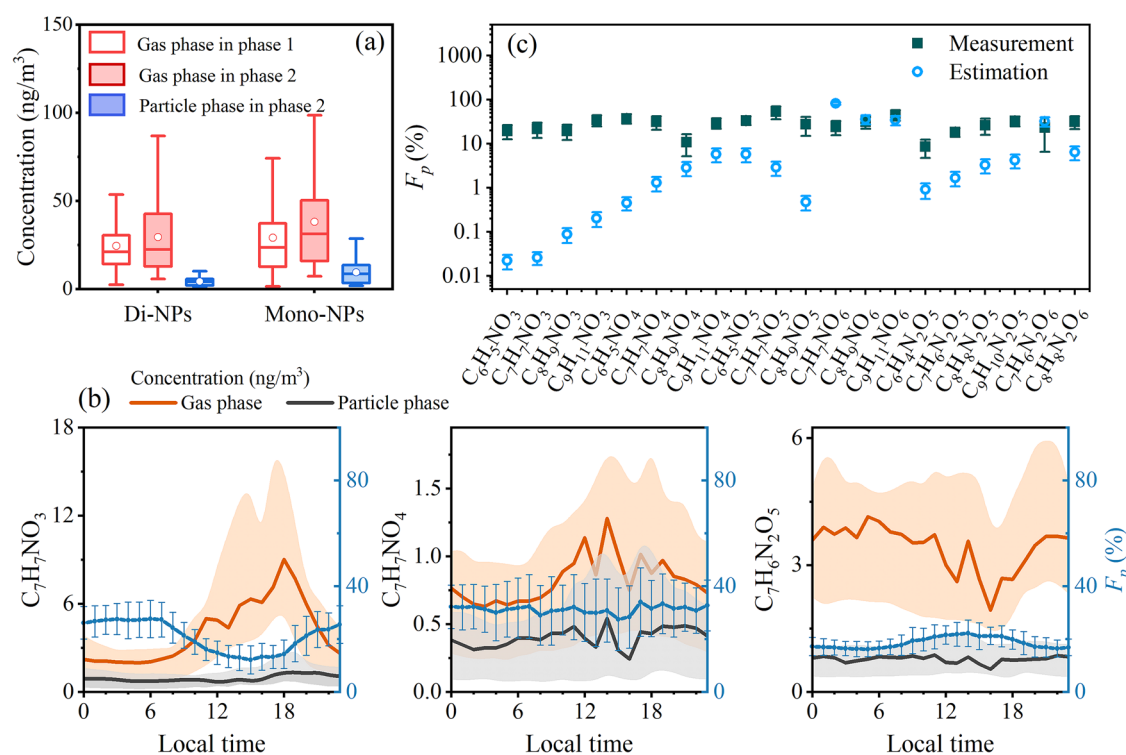


Fig. 1 | Overview of NPs partitioning observations. **a** The averaged concentration of measured gaseous and particulate NPs (mono-NPs and di-NPs); **b** The diurnal variation of concentration in the gas phase, particle phase and the fraction in the

particle of $C_7H_7NO_3$, $C_7H_7NO_4$, and $C_7H_6N_2O_5$; **c** The measured and absorption equilibrium theory estimated F_p of NPs.

Table 1 | The fitted activity coefficient ζ of studied compounds in this study

Compound	ζ	F_p peak	Compound	ζ	F_p peak	Compound	ζ	F_p peak
C ₆ H ₅ NO ₃	0.0010	N	C ₆ H ₅ NO ₅	0.11	None	C ₆ H ₄ N ₂ O ₅	0.12	D
C ₇ H ₇ NO ₃	0.0014	N	C ₇ H ₇ NO ₅	0.018	None	C ₇ H ₆ N ₂ O ₅	0.074	D
C ₈ H ₉ NO ₃	0.0039	N	C ₈ H ₉ NO ₅	0.0077 (D)	D	C ₈ H ₈ N ₂ O ₅	0.10	D
C ₉ H ₁₁ NO ₃	0.0041	N		0.027 (N)		C ₉ H ₁₀ N ₂ O ₅	0.071	None
C ₆ H ₅ NO ₄	0.0064	None	C ₇ H ₇ NO ₆	9.8 (D)	D	C ₇ H ₆ N ₂ O ₆	0.51 (D)	D
C ₇ H ₇ NO ₄	0.021	None		23.3 (N)			6.7 (N)	
C ₈ H ₉ NO ₄	0.34	None	C ₈ H ₉ NO ₆	1.04	None	C ₈ H ₈ N ₂ O ₆	0.086 (D)	D
C ₉ H ₁₁ NO ₄	0.13	None	C ₉ H ₁₁ NO ₆	0.57	None		0.23 (N)	

F_p peak summarizes the peak appearance time of F_p , where D and N represent daytime and nighttime, respectively.

(C₆₋₉H_xN₂O₅, C₇₋₈H_xN₂O₆) were identified and measured in the field campaign (Fig. 1a, S1, and Table S1)³⁶. Gaseous NPs were measured by ToF-CIMS with gas inlet from 6 October to 24 November 2020 (Phase 1), and gaseous and particulate NPs were concurrently measured with the FIGAERO inlet from 26 November to 19 December 2020 (Phase 2).

Most of the measured NPs showed a good correlation between the gas and particle phases (Fig. S2a). Besides, individual NP strongly correlated with each other in the particle phase, and also with PM_{2.5} and BrC (Fig. S2b). The average concentration of total measured gaseous NPs during the whole campaign was 58.0 ± 36.6 ng/m³ with mono-NPs of 32.0 ± 25.7 ng/m³ and di-NPs of 26.1 ± 17.4 ng/m³, which were higher than the particulate concentrations of NPs (Fig. 1a and Table S1). The average and maximum concentrations of particulate NPs were 13.8 and 45.4 ng/m³, respectively, about one-fifth and one-third of the corresponding gas phase concentration in Phase 2 (67.8 and 227.5 ng/m³). Among the measured gaseous NPs, C₆H₄N₂O₅ was the most dominant species with an average concentration of 17.68 ± 12.4 ng/m³, followed by C₆H₅NO₃ (11.18 ± 9.09 ng/m³), and C₈H₉NO₄ (7.89 ± 8.51 ng/m³) in turn. Different from the gaseous NPs, C₆H₅NO₃ showed the highest concentration (2.7 ± 2.0 ng/m³) in the particle phase, followed by C₆H₄N₂O₅ and C₇H₇NO₃, with average concentrations of 1.4 ± 0.6 ng/m³ and 1.1 ± 0.92 ng/m³, respectively. The inconsistent trend of NPs concentrations in the gas and particle phases reflected the different GPP properties across species.

As shown in Fig. 1b and S3, the diurnal variations of gaseous NPs, particulate NPs, and F_p were captured. Unexpectedly, F_p showed three types of diurnal patterns, i.e., nighttime peaks, no diurnal variation, and daytime peaks, as summarized in Table 1. Gaseous mono-NPs with only one -OH substituted group (C₆₋₉H_xNO₃) started to increase at around 8:00 and peaked at noon and afternoon, while the increase in particle phase began at 11:00 and reached the peak at around 17:00, resulting in a daytime F_p trough but higher nighttime value. NPs such as C_{6,7,9}H_xNO₄, C_{6,7}H_xNO₅, and C_{8,9}H_xNO₆ presented similar diurnal variations in the gas and particle phases, leading to a stable diurnal of F_p . C₆₋₈H_xN₂O₅ and C_{7,8}H_xN₂O₆ showed daytime troughs in the gas phase, but a slight increase or stable trend in the particle phase, resulting in higher F_p in the daytime. The diversity of F_p diurnals suggests that there are essential yet complicated processes of GPP that need to be explored.

The average F_p of NPs varied from 8.6% (C₆H₄N₂O₅) to 53% (C₇H₇NO₅) (Fig. 1c), which was comparable to the F_p measured in previous studies at urban Jinan¹¹, Mount Tai¹⁰, Beijing³⁷, Rome⁹, and Iowa³⁸ utilizing High-Performance Liquid Chromatography Mass Spectrometry (HPLC-MS), FIGAERO-CIMS, or Gas Chromatography Mass Spectrometry (GC-MS) method. The F_p of C₆H₅NO₃ ranged from 4.6% to 39% with an average value of 20%, which is a little lower than the observed F_p of 4-nitrophenol at Mount Tai (27.8% to 77%) and at Jinan (about 30% and 55% in summer and spring, respectively)^{10,11}. The measured F_p of C₆H₄N₂O₅ (3.2%–22%) was comparable to the reported F_p of 2,4-dinitrophenol at Mount Tai (1.4%–38%) and Jinan (about 5% and 35% in summer and spring, respectively)^{10,11}. However, most of the estimated F_p of NPs from absorption equilibrium theory (with the assumption of ζ being 1) are located

outside the observation range, showing discrepancies up to 4 orders of magnitude (Fig. 1c). In addition to the absorption equilibrium theory, several other theoretical methods were also used to estimate the F_p of NPs, including Junge–Pankow (J–P) adsorption model, Harner–Bidleman (H–B) K_{oa} -based absorption model, steady-state approximation model (L–M–Y model), and Linear Solvation Energy Relationship (LSER) model. Detailed information is provided in the supporting information (SI). In light of the potential impact of compound structure on the GPP process, the calculation incorporated various possible NP structures. Large discrepancies were still found for most of the estimated values compared to the observations (Fig. S4 and S5). For example, the estimated F_p values of C₆₋₉H_xNO₃ were 5.2×10^{-7} to 0.17, which was 2 to 10^5 times lower than the measurements. More results and detailed discussions are also given in the SI. The phenomenon was similar to the results reported in previous studies, showing the unmatched results between estimated and measured F_p of NPs^{10,11,39}. Although uncertainties arising from calibration, potential mixture of multiple structural isomers, and systematic errors may affect the accuracy of the measured F_p of NPs, the magnitude and consistency of the discrepancy, along with comparable results as reported in previous studies suggest that measurement uncertainties alone are unlikely to fully explain the observed differences between measured and estimated values^{9–11,37,38}. Besides, observed F_p higher than theoretical estimations were also widely reported for other multifunctional compounds in addition to NPs in previous studies, suggesting some common and large uncertainties in accounting for the GPP of oxygenated SVOCs^{8,27,39}.

Derivation of new empirical parameters

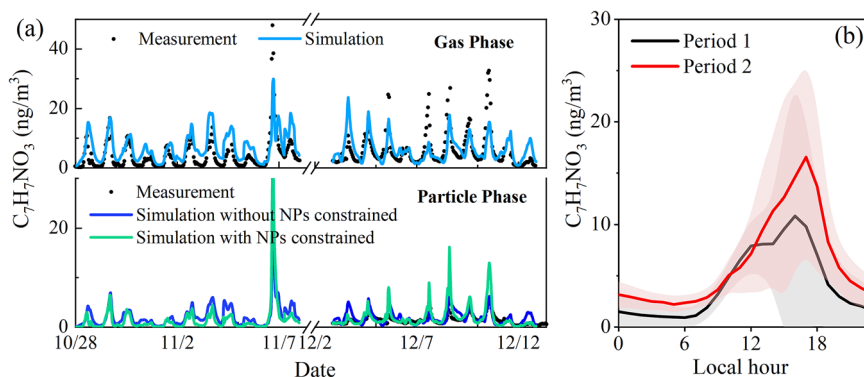
For the ideal solution/condition, the ζ in Pankow's absorption equilibrium theory can be assumed as 1 in calculating the GPP of SVOCs²². However, the nonideal behavior of mixtures of organic aerosol components has been proved, which would lead to a deviation of ζ from 1 and thus bring errors to the estimation of K_{ep} and F_p ^{25,30}.

The field measured K_{ep} could be calculated from $\frac{C_p}{C_g \times PM}$, where C_p (ng/m³), C_g (ng/m³), and PM (μg/m³) are the concentration of particulate NPs, gaseous NPs, and fine particulate matter. By integrating with Pankow's theory, the relationship between ζ and other measured parameters could be derived as Eq. 2, in which OA represents total organic matter in particles.

$$C_g = \frac{10^6 \times C_p \times P^0 \times MW_{om}}{760 \times R \times T \times OA} \times \zeta \quad (2)$$

As shown in Fig. S6, C_g of most studied NP compounds showed good correlation with $\frac{10^6 \times C_p \times P^0 \times MW_{om}}{760 \times R \times T \times OA}$, implying that ζ kept relatively stable during the field campaign. Among the studied compounds, the scatter plots of C₈H₉NO₅, C₇H₇NO₆, C₇H₆N₂O₆, and C₈H₈N₂O₆ showed two branches, and good correlations between C_g and $\frac{10^6 \times C_p \times P^0 \times MW_{om}}{760 \times R \times T \times OA}$ still existed in each branch, corresponding to daytime and nighttime data (Fig. S7). Then, an apparent effective value of ζ can be fitted. The derived ζ of studied NPs are

Fig. 2 | Observed and simulated $C_7H_7NO_3$ during the campaign. a The simulated and measured $C_7H_7NO_3$ in gas and particle phases; **b** The diurnal variation of measured gaseous $C_7H_7NO_3$ during 28 October to 8 November (period 1) and 3 December to 13 December (period 2).



summarized in Table 1 with most of the fitted values lower than 1. For example, the fitted ζ of $C_{6-9}H_xNO_3$ ranged from 0.001 to 0.0041, which is 2 to 3 orders of magnitude lower than 1. It should be noted that the apparent parameter ζ may also encompass the potential uncertainties from P^0 estimation with Estimation Programs Interface (EPI) suite^{40,41}, which is a Windows-based suite of physical/chemical property and environmental fate estimation programs developed by EPA and Syracuse Research Corp. However, due to the lack of P^0 measurement, theoretical estimations remain the only feasible approach and have been widely used in previous studies. More accurate ζ values can be refined as experimental P^0 data become available in the future. More detailed discussion about P^0 and the sensitivity of F_p towards the change of ζ for different species could be found in SI. The branching behavior of $C_8H_9NO_5$, $C_7H_7NO_6$, $C_7H_6N_2O_6$, and $C_8H_8N_2O_6$ suggests differences in GPP processes between day and night. The variability in the physicochemical properties (such as differences in acidity and viscosity) of organic aerosols influenced by air mass origin may influence the GPP process. However, the backward trajectory analysis showed no clear dependence of the pattern on air mass clusters. Then, it is speculated that the observed variations in ζ are likely caused by the different formation pathways and/or different molecular structures for them during day and night. Besides, disregarding uncertainties associated with P^0 and other parameters, the high ζ values for $C_7H_7NO_6$ and $C_7H_6N_2O_6$ observed at nighttime may suggest the occurrence of phase separation; however, further evidence and additional studies are required to substantiate this hypothesis.

In addition to the possible overestimation of P^0 , the low ζ of NPs might be contributed by the strong interactions between NPs and other components in the aerosol, such as hydrogen bond⁴². If the interaction between NPs and other aerosol components was stronger than the interaction of NPs in pure sub-cool liquid, the escape of NPs from aerosol would be harder than that from pure NPs, leading to a higher F_p and lower ζ of NPs in the real atmosphere than that in the ideal state. The NPs molecules contain $-OH$, $-NO_2$, and benzene ring in their structures, which could act as hydrogen bond acceptors and donors at the same time. Highly oxygenated organic molecules generated from RO_2 autoxidation and oligomers have been identified as dominant components contributing to secondary aerosol formation^{1,2}. Many $-OOH$, $-C(O)O-$, and $-OH$ functional groups in their structures can interact with NPs by hydrogen bond. If the interactions between aerosol components and NPs are higher than those between NPs themselves, more NPs would distribute in the aerosol phase than the ideal state, resulting in ζ lower than 1⁴³. Similar reasons could also explain the previously reported higher observed F_p than estimations for multifunctional compounds^{8,27,39}.

Furthermore, it is found that for mono-NPs ($C_xH_yNO_3$ and $C_xH_yNO_4$) with the same oxygen content, an increase in the number of carbon atoms corresponds to a rise in their ζ values (Table 1 and Fig. S8). This trend is consistent with the findings of Donahue et al.⁴⁴ and may be partly attributed to the reduced molecular polarity due to additional $-CH_3$ groups. In contrast, no clear trend was observed for di-NPs. Although the addition of a second $-NO_2$ group increases molecular polarity, di-NP often exhibited even higher apparent activity coefficients than their mono-NP counterparts. This

result may reflect not only solute properties but also the interaction between solute and aerosol-phase solvent. According to the results of Donahue et al.⁴⁴, a smaller difference in O:C ratio between them would yield a smaller deviation from ideal behavior. Therefore, it is plausible that the bulk aerosol composition is more chemically similar to the di-NPs than to mono-NPs, thereby minimizing solute-solvent mismatch and contributing to the higher apparent ζ values observed for di-NPs. While this interpretation is consistent with existing theoretical frameworks, we acknowledge that it remains speculative. Additional experimental studies are needed to quantify how functional group additions, molecular polarity, and bulk aerosol composition collectively influence activity coefficients under atmospherically relevant conditions.

Application of derived parameter in model mechanistic analysis

An OBM embedded with GPP module was used to simulate the formation and processing of NPs in both gas and particle phases. The derived ζ value instead of 1 was adopted in the OBM. Considering the availability of necessary pollutants and parameters for model input, NPs in period 1 (28 October to 8 November) and period 2 (3 December to 13 December) were simulated to represent Phase 1 and Phase 2, respectively. As shown in Fig. 2a and S9a, the OBM could well reproduce the temporal variations of gaseous $C_6H_5NO_3$, $C_7H_7NO_3$, and $C_8H_9NO_3$ in period 1. Comparable gaseous $C_7H_7NO_3$ and slightly lower concentrations of gaseous $C_6H_5NO_3$ and $C_8H_9NO_3$ than the observations were simulated in period 2. Regarding the particle phase, the simulated $C_7H_7NO_3$ in period 2 was comparable to the measurement, while simulations were relatively lower than the observations for $C_6H_5NO_3$ and $C_8H_9NO_3$ (Fig. S9b). When gaseous mono-NPs concentrations were constrained in the model, the simulated particulate mono-NPs showed improved agreement with observations. These results demonstrate the applicability of the embedded GPP module and field-derived average ζ value. Particulate mono-NPs in Period 1 were also estimated based on the measured gaseous mono-NPs, with peak concentrations of $C_6H_5NO_3$, $C_7H_7NO_3$, and $C_8H_9NO_3$ up to 23.1, 37.2, and 11.7 ng/m³, respectively. We further examined whether the derived ζ can be directly used to estimate the concentration of gaseous/particulate NPs from Eq. 2 by the known concentration in another phase. Unsurprisingly, the calculated C_g diurnal variations of compounds such as $C_{6-9}H_xNO_3$ with nighttime F_p peaks were similar to their measurements (Fig. S10), indicating mathematical calculations from Eqs. 1 and 2 with the derived ζ can also estimate G-P partitioning of some species effectively.

It is worth noting that the observed peak time of gaseous $C_{6-8}H_xNO_3$ in period 1 showed earlier than that in period 2 (Fig. 2b and S11), which presented bimodal peaks at around 12:00 and 16:00 in period 1, and respectively shifted two and one hours later in period 2. The consistency between the model simulation and observation implies that the peak shift is well captured by the photochemical mechanisms and embedded GPP process in the model. The budget analysis of $C_7H_7NO_3$ is discussed as an example. As shown in Fig. 3a, b and Scheme S1, the gaseous $C_7H_7NO_3$ formation was mainly from 3-methyl-phenoxy (MXYL10), 4-methyl-phenoxy (PXYL10) and 2-methyl-phenoxy (TOL10) reacting

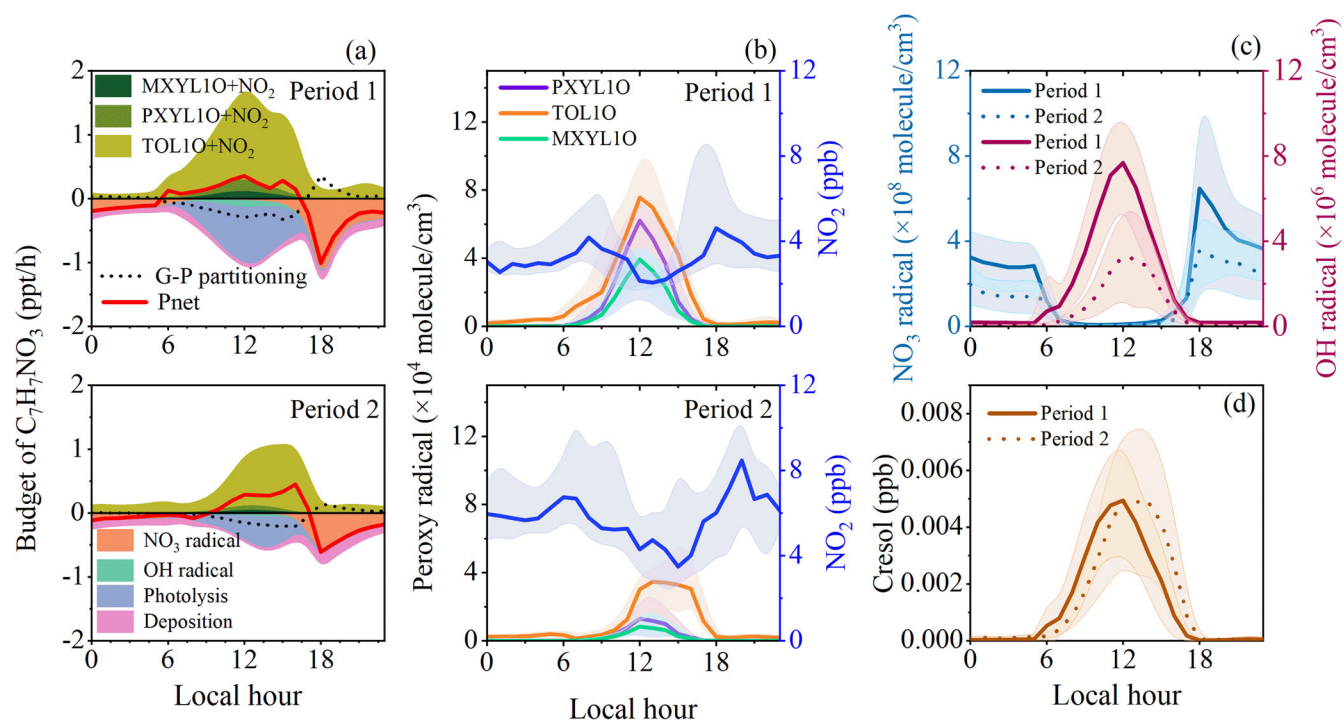


Fig. 3 | Budget analysis of $C_7H_7NO_3$ and diurnal variations of key species. The gaseous $C_7H_7NO_3$ budget (a), phenoxy radical and NO_2 diurnal (b), diurnal patterns of OH and NO_3 radical (c), and diurnal of cresol (d) in period 1 and period 2.

with NO_2 , with average contributions of 2.5%, 4.0%, and 93.5% in period 1 and 1.7%, 2.7% and 95.6% in period 2, respectively. As the dominant precursor for gaseous $C_7H_7NO_3$, TOLIO was generated from cresol oxidation by OH radical and NO_3 radical, *o*-methylphenyl peroxide (OXYLIO2) reacting with NO , NO_2 , and RO_2 , and the photolysis of OXYLIOOH (Fig. S12a and S12b). The contribution of the photolysis of OXYLIOOH was negligible in the present study. Although OXYLIO2 reacting with NO could contribute to a large formation rate of TOLIO, the reaction between TOLIO and O_3 could quickly recycle OXYLIO2 with similar rates, leading to a small net formation rate of TOLIO from OXYLIO2. The cresol oxidation by NO_3 and OH dominated TOLIO formation, with a total rate up to 1.4 and 1.2 ppt/h during period 1 and period 2, respectively. Similar to our previous study, the contribution of NO_3 +cresol was more important than OH+cresol to the TOLIO formation, which can be explained by the comparable reaction rates, but a much higher yield of TOLIO from NO_3 (39%) than OH (7.3%)³⁶. Dominated by the photooxidation of toluene, the cresol concentration started to increase after sunrise and peaked at noontime. Attributed to the stronger and longer irradiation in period 1 than in period 2 (Fig. S12c), higher concentration of OH radicals with earlier peak time were observed in period 1 (Fig. 3c), resulting in the earlier cresol formation in period 1 than in period 2 (Fig. 3d). The combined effects of postponed cresol formation and lower OH concentrations in period 2, resulted in the late and less formation of TOLIO, PXYLIO, and MXYLIO, and thus the delayed formation of gaseous $C_7H_7NO_3$ with a lower formation rate.

$C_7H_7NO_3$ could be further photolyzed and oxidized by OH/ NO_3 radicals. The photolysis contributed over 80% of $C_7H_7NO_3$ consumption during 9:00–15:00 in both periods, with the highest photolysis rate of 0.9 ppt/h at 13:00 for period 1 and 0.5 ppt/h at 14:00 for period 2, respectively. Further OH radical oxidation contributed 6.7% and 3.3% to daytime $C_7H_7NO_3$ consumption in period 1 and period 2, respectively. NO_3 radical oxidation was the dominant sink for $C_7H_7NO_3$ at night and accounted for 67% and 53% of nocturnal consumption with the highest consumption rate of 1.3 and 0.7 ppt/h at 18:00 in period 1 and period 2, respectively. Besides the chemical sinks, dry deposition also contributed 28% and 42% of gaseous $C_7H_7NO_3$ nighttime loss in period 1 and period 2, respectively. The GPP served as a daytime sink but a nighttime source for gaseous $C_7H_7NO_3$. The

rapid daytime secondary generation of gaseous $C_7H_7NO_3$ drove the GPP equilibrium shift towards the particle phase, whereas fast consumption by NO_3 oxidation during nighttime resulted in more particle-to-gas release of $C_7H_7NO_3$. Offset by the consumption pathways, the net formation rate of gaseous $C_7H_7NO_3$ ($P_{net-C_7H_7NO_3}$) showed positive values during 6:00–16:00 and 10:00–17:00 in period 1 and period 2, respectively, resulting in the diurnal peak shift of gaseous $C_7H_7NO_3$ in two periods. Similar processes and reasons can also explain the observed diurnal peak shift of gaseous $C_6H_5NO_3$ and $C_8H_9NO_3$ in the two observation periods.

Unexpected complex GPP of di-NPs

The oxidation of gaseous mono-NPs by OH and NO_3 radicals is a major formation pathway for gaseous di-NPs in the OBM. Compared to observation, the model simulated temporal trends of gaseous di-NPs are not as good as mono-NPs. Gaseous $C_7H_6N_2O_5$ and $C_8H_8N_2O_5$ showed almost consistent results as observations in period 2, but gaseous $C_6H_4N_2O_5$ was underestimated (Figure S13), suggesting the important role of the oxidation of gaseous mono-NPs on their formation, and also the existence of missing sources. Unlike the nighttime peaks observed in period 2 and previous studies, gaseous $C_6H_4N_2O_5$, $C_7H_6N_2O_5$ and $C_8H_8N_2O_5$ presented morning peaks around 6:00 to 10:00 in period 1 (Fig. S14), which could be explained by the physical transportation, resulting in the inconsistency between model simulation and observation. More discussions are presented in the SI.

Regarding the particulate di-NPs, their time series cannot be reproduced from the model simulation, even when the gaseous di-NPs were constrained in the model (Fig. S13b). It suggests that the simple GPP parameterization in the model cannot represent the complex gas-particle interaction of di-NPs. It is observed that measured particulate $C_{6-8}H_xN_2O_5$ showed daytime peaks during the field campaign, especially from 27 November to 3 December (Figs. 4a and S15a). The fast growth of gaseous $C_{6-8}H_xN_2O_5$ in the night, and the particulate $C_{6-8}H_xN_2O_5$ in the daytime might be attributed to the varied contributions of different formation mechanisms. It has been proposed that mono-NPs could react with the nitrite/nitrous acid ($NO_2^-/HONO$) in the aqueous phase under irradiation conditions and contribute to di-NPs formation⁴⁵. The accompanied increase of particulate $C_{6-8}H_xNO_3$ in the daytime provided the potential

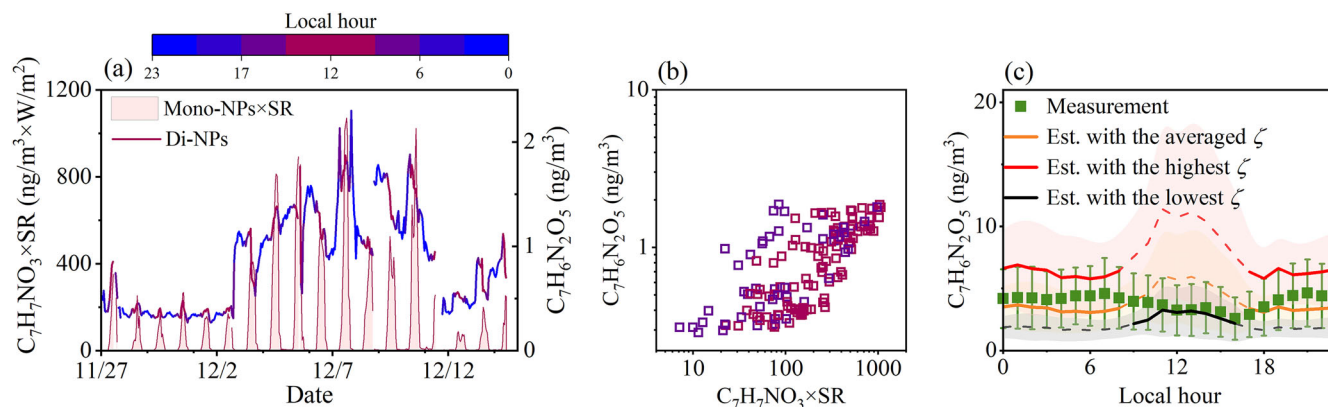


Fig. 4 | Formation and phase partitioning of $C_7H_6N_2O_5$. **a** Time series of measured particulate $C_7H_6N_2O_5$ and the product of measured particulate $C_7H_7NO_3 \times SR$; **b** Scatter plot of measured particulate $C_7H_6N_2O_5$ as a function of the product of

measured particulate $C_7H_7NO_3 \times SR$ during the daytime; **c** Comparison of the calculated gaseous $C_7H_6N_2O_5$ from Eq. 2 with fitted the lowest, highest, and averaged ζ and the measured gaseous $C_7H_6N_2O_5$.

precursors for the formation of particulate $C_{6-8}H_xN_2O_5$. Thus, we examined the correlation between measured particulate $C_{6-8}H_xN_2O_5$ and particulate $C_{6-8}H_xNO_3 \times SR$ in the daytime. The good correlation, as shown in Fig. 4a, b and S15, suggests that the photo-enhanced particulate reactions potentially contributed to particulate $C_{6-8}H_xN_2O_5$ formation in the daytime, which would further distribute to the gas phase. In contrast, the gaseous $C_{6-8}H_xN_2O_5$ formation at night was dominated by the NO_3 oxidation of gaseous $C_{6-8}H_xNO_3$, and then partitioning into the particle phase.

Under ideal conditions, the GPP coefficient should be the same no matter the phase from which the compounds originated. However, the results show that compounds in the real atmosphere tended to partition more into the phase they generated in compared to the ideal state, namely a hysteresis effect, which might reflect a non-equilibrium state of GPP, possibly influenced by kinetic limitations, delayed mixing, or phase-dependent transformation processes^{46–48}. The daytime particulate formation and nighttime gaseous accumulation resulted in a lower ζ in the daytime and the daytime peak of F_p for $C_{6-8}H_xN_2O_5$. Because $C_{6-9}H_xNO_3$ were dominated by gaseous oxidation, their time series could be better reproduced from OBM that only includes the gas phase reactions, and their F_p diurnal patterns could be well explained by Pankow's theory with fitted ζ . However, for species like $C_{6-8}H_xN_2O_5$ that are involved in both gaseous and particulate formation pathways, the OBM model cannot reproduce their time series, especially in the particle phase. Additionally, for NPs such as $C_7H_7NO_6$, which exhibit different fitted ζ values during daytime and nighttime (Table 1), a decrease in gas-phase concentrations and a slight increase in particle-phase concentrations were observed during the day (Fig. S3). This suggests that, in addition to significant gaseous formation occurring in the evening, photochemical reactions during the day may also contribute to the particulate formation of these NPs. These differences in formation pathways likely contribute to the differing ζ values obtained between daytime and nighttime. Given the complex particulate reactions, such as accretion and photochemical processes, that occur concurrently with gaseous reactions in the ambient atmosphere, it is likely that the compounds associated with these reactions undergo a more intricate GPP process than previously acknowledged^{49–52}. The measurement of GPP with high time resolution is helpful to reveal the complex reaction mechanisms behind the apparent phenomena.

The mathematically calculated gaseous $C_{6-8}H_xN_2O_5$ from Eq. 2 also showed different diurnal variations from the measurements (Figs. 4c and S10). The field-derived maximum and minimum ζ were further fitted from the highest and lowest 20% ratio of C_g of di-NPs to $\frac{10^6 \times C_p \times P^0 \times MW_{om}}{760 \times RT \times OA}$, which were 0.5 to 2 times of the averaged ζ (Fig. S16). If the highest and lowest ζ values were used in the calculation, the calculated C_g would peak in the daytime, different from the observed daytime valley (Figs. 4c and S17). When dividing the diurnal into two parts, i.e., 9:00–16:00 and the remaining part, it is found that the value and trend of the calculated C_g

from the lowest ζ in the noontime was closer to the measurement, while C_g more comparable to the measurement was observed during nighttime when using the averaged ζ . These phenomena are consistent with the analysis above that there is a lower ζ in the daytime for di-NPs. Besides, these results also suggest that more refined ζ corresponding to different chemical pathways is needed to describe the GPP of compounds generated from both gas and particle phases more precisely.

Atmospheric implications

By incorporating the derived ζ into the Pankow's absorption equilibrium theory, we first recalculated the average F_p values for NPs observed in this study. As expected, these reconstructed values closely matched the measurement (Fig. 5a), serving to demonstrate the internal consistency of the approach. More importantly, the newly fitted ζ values were further utilized to estimate F_p in previous studies to evaluate their applicability in different situations (Fig. 5b). The estimated F_p values using the fitted ζ for 4-nitrophenol (4NP), 3-methyl-4-nitrophenol (3M4NP), 2-methyl-4-nitrophenol (2M4NP), 2,6-dimethyl-4-nitrophenol (2,6DM4NP), and 4-nitrocatechol (4NC) were found to align well with their observation ranges reported by Li et al.¹⁰. Similar results with improved estimation of F_p can also be obtained for I.M. Al-Naiema's results³⁸. The strong agreement of F_p with the measured values suggests that, although the fitted ζ values were obtained from a subtropical coastal site, they have great potential for broader application in other regions.

To further explore the effectiveness of the apparent ζ and Pankow's absorption equilibrium on GPP of NPs, a GEOS-Chem global 3-D chemical transport model (v12.9.3) with a resolution of 5° longitude \times 4° latitude and 72 vertical layers was applied to simulate NPs formation worldwide. This model has been successfully used to assess the contributions of organic nitrogen aerosols to global atmospheric nitrogen deposition²¹. Field observation data reported in previous studies covering the locations of latitudes from 22.2° to 55.3° and longitudes from -118.12° to 136.92° were used for comparison (Table S2). As shown in Fig. 5c, the simulated particulate NPs were mostly within one order of magnitude of the measurement values, underscoring the practical applicability of the derived apparent ζ and Pankow's theory in describing the GPP of NPs across different regions. Accurate simulation of particulate NPs is essential for estimating their contribution to aerosol formation and evaluating their roles in solar radiation. Additionally, the method for deriving apparent ζ from field measurement can be applied to other SVOCs, providing a promising approach to improve the model performance in simulating the GPP of SVOCs and further exploring their impacts on aerosol formation and air quality.

Besides, it was observed that the derived ζ decreased with the increase of P^0 , following a relationship of $\text{Log } \zeta = -0.91 \times \text{Log } P^0 - 3.3$ (Fig. 5d). This suggests that the ζ value for compounds with similar structures could be

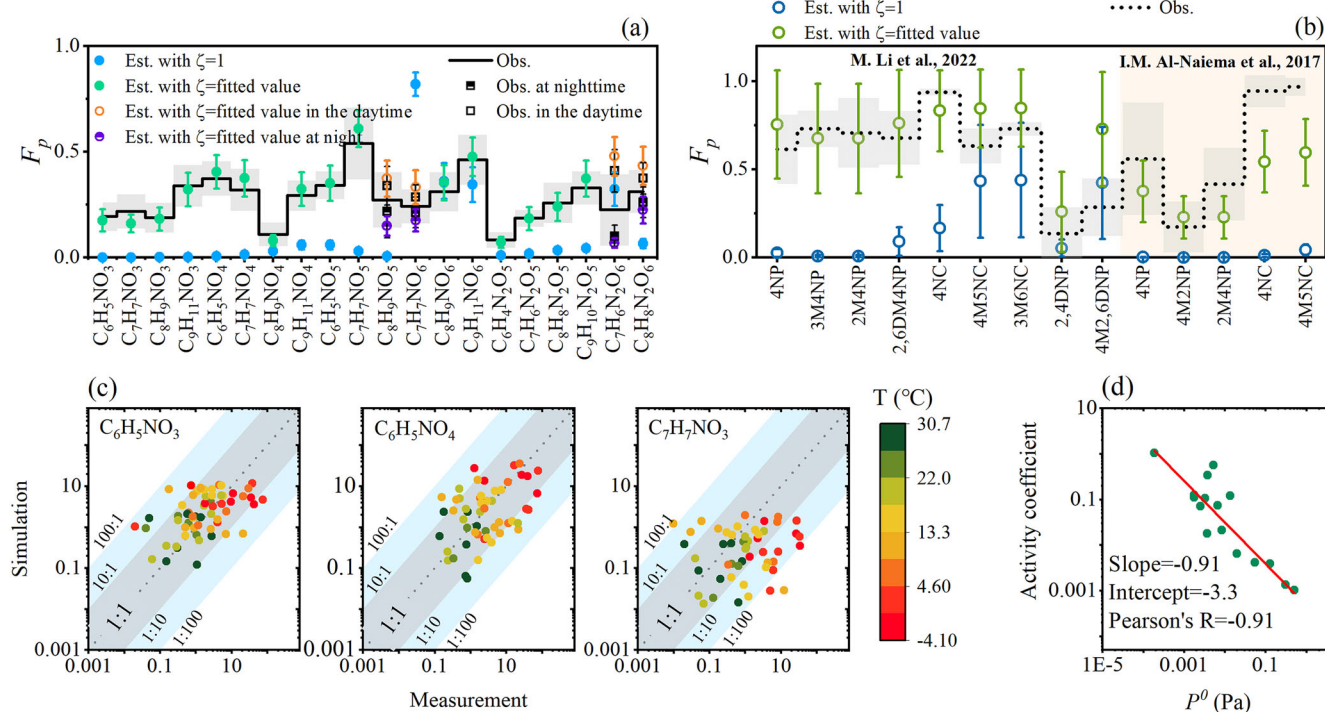


Fig. 5 | Application of the derived ζ in measurements and modeling. The comparison of F_p between the observation and the estimation with $\zeta = 1$ and $\zeta =$ fitted value in our (a) and previous studies (b); c Comparison of particulate NPs (ng/m^3)

between the observation and GEOS-Chem model simulation with derived apparent ζ , and d the derived ζ as a function of P^0 .

estimated accordingly, opening avenues for measuring and estimating the ζ value for other types of SVOCs. Utterly, it is promising that utilizing their newly fitted or estimated ζ value could enhance the performance of regional models in simulating SVOCs distributions, investigating their contributions to OA formation and understanding their impacts on air quality. Nevertheless, some considerations are warranted. Uncertainties from the theoretical estimation of P^0 were included in the apparent ζ due to a lack of accurate measurement values, however, systematic revisions can be made when accurate P^0 is measured in the future. The obtained ζ values here represent an average value for isomeric compounds with different structures, and the specific structure variations may lead to higher or lower ζ values. Furthermore, different atmospheric conditions might introduce the unknown deviations in ζ . Given the wide application of GPP theory in estimating the distributions of SVOCs in various models, the potential underestimation of F_p for most oxygenated SVOCs caused by the oversimplified ζ assumption would underrate the significance of oxygenated SVOCs in global/regional climate and air quality. Therefore, a more quantitative understanding of ζ is necessary to accurately evaluate the role of SVOCs in atmospheric chemistry.

Methods

Measurement of NPs and other key precursors and parameters

Data presented here were collected at a regional background monitoring station (Cape D'Aguilar, 22.22°N, 114.25°E), which is located on the southeastern tip of Hong Kong Island, surrounded by sea on three sides and about 10 km from the nearest urban center⁵³. The continuous field campaign was conducted in autumn to winter (from 6 October to 19 December) in 2020, which was the period with more frequent photochemical pollution in Hong Kong.

An Iodide-adduct ToF-CIMS was used to measure targeted NPs. Only the gas inlet was used from 6 October to 24 November (Phase 1), and FIGAERO was installed on 26 November (Phase 2) to concurrently measure gaseous and particulate NPs till the end of the field campaign. The primary reagent ion of Γ was produced by passing the CH_3I and humid carrier gas N_2

through an inline ionizer (^{210}Po). The relative humidity (RH) of the carrier gas was kept at around 50% to maintain a stable ratio between Γ and $I\cdot H_2O^+$. The pressure of the IMR was set to 100 mbar, leading to a sample flow of 2.5 L/min. When the FIGAERO inlet was used, aerosols with a size smaller than 3 μm were pumped through a cyclone cutting head with a flow rate of 10 L/min and continuously collected on the Teflon filter for 25 min, meanwhile, the gaseous pollutants were analyzed by ToF-CIMS concurrently. Then, a thermal desorption program described in the SI was applied to analyze the NPs collected on the filter. During each cycle of sample collection and analysis (1 h), 25 min was used for the gaseous sample analysis, and a total of 35 min was used to analyze the particulate sample that was collected at the same time as the gaseous sample. The concentration of NPs was calibrated by the obtained calibration coefficients as described in SI. Briefly, NPs standards including 2-methyl-4-nitrophenol, 2,6-dimethyl-4-nitrophenol, and 3,6-dimethyl-2,4-dinitrophenol were added to the filter, and analyzed with the same thermal desorption program as ambient sample analysis, then calibration coefficients could be obtained. Detailed information on data analysis and other instruments can be found in the SI.

Calculation and theoretical estimation of F_p

The F_p of species i is defined as Eq. 3,

$$F_p = \frac{C_p}{C_g + C_p} \quad (3)$$

where C_p (ng/m^3) and C_g (ng/m^3) are the concentrations of species i in the particle and gas phase, respectively. K_{ep} could be calculated from Eq. 4, where PM represents the $PM_{2.5}$ concentration ($\mu g/m^3$), and could also be estimated from theory: Eq. 1.

$$K_{ep} = \frac{C_p}{C_g \times PM} \quad (4)$$

Both adsorption and absorption are reported to be important pathways for gaseous SVOCs to enter the particle phase, while they are more significant for gaseous SVOCs partitioning on solid and liquid aerosol, respectively. Because of the most likely liquid state for most of the aerosol caused by high RH during the period (average RH: 71% and the frequency of RH larger than 60% was over 84%), the GPP of NPs in the gas and particle phase was assumed to be led by the absorption process⁵⁴. The most typical theory of SVOC absorbed in particles is the absorption equilibrium theory developed by Pankow as shown in Eq. 1²². Thus, the F_p could be described by Eq. 5 by incorporating the estimated K_{ep} .

$$F_p = \frac{K_{ep} \times PM}{1 + K_{ep} \times PM} \quad (5)$$

Besides Pankow's absorption equilibrium theory, several other theoretical methods have also been used to estimate the F_p of NPs^{5,55}. Detailed discussions of these theoretical methods are presented in SI.

Model simulations

An OBM built on the Master Chemical Mechanism (MCM v3.3.1) (<http://mcm.york.ac.uk>)^{56,57} was employed to analyze the budget of the observed NPs^{15,36}, which is described in detail in SI and our previous study³⁶. Briefly, the OBM incorporates inorganic and organic reaction mechanisms from MCM 3.3.1, supplemented with additional processes including the photolysis of gaseous and particulate NPs, dry deposition, and the GPP of NPs. In the model, 1.4% and 3% of the photolysis rate of NO₂ (JNO₂) were respectively adopted as the photolysis rate for nitrophenol and other NPs in both gas and particle phases, based on our previous findings³⁶. Dry deposition rates for NPs in both gas and particle phases and other reactive species were set within a range of (0.550~1)/HMIX (HMIX: height of mixing layer), following the approach used in previous work⁵⁸. A GPP module, following Johnson et al.⁵⁹, was embedded in the model by coupling with the derived ζ for targeted NPs. The dynamical process of GPP could be treated as a reversible reaction with an absorption process (k_{in}) and a desorption process (k_{out})⁵⁹. Detailed mechanisms for targeted NPs in the OBM are provided in the SI. The model simulations were conducted for two periods: 26 October to 8 November (period 1) and 3 to 12 December (period 2), during which the OBM was constrained with observational data including trace gases, key VOC species, N₂O₅, and meteorological parameters. Besides, a GEOS-Chem global 3-D chemical transport model (v12.9.3, <http://geos-chem.org>) embedded with the GPP module was used to simulate the NPs formation in different regions. Except for the updated parameters in the GPP module, the basic settings of the model were the same as before, which can be found in our previous study²¹.

Data availability

Data is provided within the manuscript or supplementary information files.

Received: 21 February 2025; Accepted: 26 June 2025;

Published online: 11 July 2025

References

- Kalberer, M. et al. Identification of polymers as major components of atmospheric organic aerosols. *Science*, 1659–1662 (2004).
- Nie, W. et al. Secondary organic aerosol formed by condensing anthropogenic vapours over China's megacities. *Nat. Geosci.* **15**, 255–261 (2022).
- Chen, Q., Fu, T.-M., Hu, J., Ying, Q. & Zhang, L. Modelling secondary organic aerosols in China. *Natl Sci. Rev.* **6**, 806–809 (2017).
- Li, J. et al. Impacts of water partitioning and polarity of organic compounds on secondary organic aerosol over eastern China. *Atmos. Chem. Phys.* **20**, 7291–7306 (2020).
- Wei, W. et al. Distributions of the particle/gas and dust/gas partition coefficients for seventy-two semi-volatile organic compounds in indoor environment. *Chemosphere* **153**, 212–219 (2016).
- Qin, C. et al. Gas–particle partitioning of polyol tracers at a suburban site in Nanjing, east China: increased partitioning to the particle phase. *Atmos. Chem. Phys.* **21**, 12141–12153 (2021).
- Xie, M., Hannigan, M. P. & Barsanti, K. C. Gas/particle partitioning of n-alkanes, PAHs and oxygenated PAHs in urban Denver. *Atmos. Environ.* **95**, 355–362 (2014).
- Williams, B. J., Goldstein, A. H., Kreisberg, N. M. & Hering, S. V. In situ measurements of gas/particle-phase transitions for atmospheric semivolatile organic compounds. *Proc. Natl Acad. Sci. USA* **107**, 6676–6681 (2010).
- Cecinato, A., Di Palo, V., Pomata, D., Tomasi Sciano, M. C. & Possanzini, M. Measurement of phase-distributed nitrophenols in Rome ambient air. *Chemosphere* **59**, 679–683 (2005).
- Li, M. et al. Atmospheric nitrated phenolic compounds in particle, gaseous, and aqueous phases during cloud events at a mountain site in North China: Distribution characteristics and aqueous-phase formation. *J. Geophys. Res.: Atmos.* **127**, e2022JD037130 (2022).
- Li, M. et al. Nitrated phenols and the phenolic precursors in the atmosphere in urban Jinan, China. *Sci. Total Environ.* **714**, 136760 (2020).
- Yuan, B. et al. Secondary formation of nitrated phenols: insights from observations during the Uintah Basin Winter Ozone Study (UBWOS) 2014. *Atmos. Chem. Phys.* **16**, 2139–2153 (2016).
- Iinuma, Y., Böge, O., Gräfe, R. & Herrmann, H. Methyl-nitrocatechols: atmospheric tracer compounds for biomass burning secondary organic aerosols. *Environ. Sci. Technol.* **44**, 8453–8459 (2010).
- Wang, Y. et al. The formation of nitro-aromatic compounds under high NO_x and anthropogenic VOC conditions in urban Beijing, China. *Atmos. Chem. Phys.* **19**, 7649–7665 (2019).
- Salvador, C. M. G. et al. Ambient nitro-aromatic compounds – biomass burning versus secondary formation in rural China. *Atmos. Chem. Phys.* **21**, 1389–1406 (2021).
- Palm, B. B. et al. Quantification of organic aerosol and brown carbon evolution in fresh wildfire plumes. *Proc. Natl Acad. Sci. USA* **117**, 29469–29477 (2020).
- Xie, M. et al. Light absorption of secondary organic aerosol: Composition and contribution of nitroaromatic compounds. *Environ. Sci. Technol.* **51**, 11607–11616 (2017).
- Sangwan, M. & Zhu, L. Role of methyl-2-nitrophenol photolysis as a potential source of OH radicals in the polluted atmosphere: Implications from laboratory investigation. *J. Phys. Chem. A* **122**, 1861–1872 (2018).
- Sangwan, M. & Zhu, L. Absorption cross sections of 2-nitrophenol in the 295–400 nm region and photolysis of 2-nitrophenol at 308 and 351 nm. *J. Phys. Chem. A* **120**, 9958–9967 (2016).
- Laskin, A., Laskin, J. & Nizkorodov, S. A. Chemistry of atmospheric brown carbon. *Chem. Rev.* **115**, 4335–4382 (2015).
- Li, Y. et al. Dissecting the contributions of organic nitrogen aerosols to global atmospheric nitrogen deposition and implications for ecosystems. *Natl Sci. Rev.* **10**, nwad244 (2023).
- Pankow, J. F. An absorption model of the gas/aerosol partitioning involved in the formation of secondary organic aerosol. *Atmos. Environ.* **28**, 189–193 (1994).
- Pankow, J. F. An absorption model of gas/particle partitioning of organic compounds in the atmosphere. *Atmos. Environ.* **28**, 185–188 (1994).
- Pankow, J. F. & Barsanti, K. C. The carbon number-polarity grid: A means to manage the complexity of the mix of organic compounds when modeling atmospheric organic particulate matter. *Atmos. Environ.* **43**, 2829–2835 (2009).
- Seinfeld, J. H. & Pandis, S. N. *Atmospheric chemistry and physics: from air pollution to climate change*. (John Wiley & Sons, 2016).
- Zuend, A. et al. New and extended parameterization of the thermodynamic model AIOMFAC: calculation of activity coefficients for organic-inorganic mixtures containing carboxyl, hydroxyl,

- carbonyl, ether, ester, alkenyl, alkyl, and aromatic functional groups. *Atmos. Chem. Phys.* **11**, 9155–9206 (2011).
27. Isaacman-VanWertz, G. et al. Ambient gas-particle partitioning of tracers for biogenic oxidation. *Environ. Sci. Technol.* **50**, 9952–9962 (2016).
 28. Healy, R. M. et al. Gas/particle partitioning of carbonyls in the photooxidation of isoprene and 1,3,5-trimethylbenzene. *Atmos. Chem. Phys.* **8**, 3215–3230 (2008).
 29. Liang, Y. et al. Gas-particle partitioning of semivolatile organic compounds when wildfire smoke comes to town. *Atmos. Chem. Phys.* **23**, 12441–12454 (2023).
 30. Cappa, C. D., Lovejoy, E. R. & Ravishankara, A. R. Evidence for liquid-like and nonideal behavior of a mixture of organic aerosol components. *Proc. Natl Acad. Sci. USA* **105**, 18687–18691 (2008).
 31. Roldin, P. et al. Modelling non-equilibrium secondary organic aerosol formation and evaporation with the aerosol dynamics, gas- and particle-phase chemistry kinetic multilayer model ADCHAM. *Atmos. Chem. Phys.* **14**, 7953–7993 (2014).
 32. Saleh, R. & Khlystov, A. Determination of activity coefficients of semi-volatile organic aerosols using the integrated volume method. *Aerosol Sci. Technol.* **43**, 838–846 (2009).
 33. Hilditch, T. G., Hardy, D. A., Stevens, N. J., Glover, P. B. & Reid, J. P. Single-particle measurements and estimations of activity coefficients for semi-volatile organic compounds in organic aerosol of known chemical speciation. *Environ. Sci.: Atmos.* **3**, 931–941 (2023).
 34. Cappa, C. D. & Wilson, K. R. Evolution of organic aerosol mass spectra upon heating: implications for OA phase and partitioning behavior. *Atmos. Chem. Phys.* **11**, 1895–1911 (2011).
 35. Liu, X., Day, D. A., Krechmer, J. E., Ziemann, P. J. & Jimenez, J. L. Determining activity coefficients of SOA from isothermal evaporation in a laboratory chamber. *Environ. Sci. Tech. Lett.* **8**, 212–217 (2020).
 36. Chen, Y. et al. Secondary formation and impacts of gaseous nitrophenolic compounds in the continental outflow observed at a background site in South China. *Environ. Sci. Technol.* **56**, 6933–6943 (2022).
 37. Le Breton, M. et al. Online gas- and particle-phase measurements of organosulfates, organosulfonates and nitrooxy organosulfates in Beijing utilizing a FIGAERO ToF-CIMS. *Atmos. Chem. Phys.* **18**, 10355–10371 (2018).
 38. Al-Naiema, I. M. & Stone, E. A. Evaluation of anthropogenic secondary organic aerosol tracers from aromatic hydrocarbons. *Atmos. Chem. Phys.* **17**, 2053–2065 (2017).
 39. Hu, H. et al. Sources and gas-particle partitioning of atmospheric parent, oxygenated, and nitrated polycyclic aromatic hydrocarbons in a humid city in southwest China. *Atmos. Environ.* **206**, 1–10 (2019).
 40. Chen, Y. et al. Effect of NO₂ on nocturnal chemistry of isoprene: Gaseous oxygenated products and secondary organic aerosol formation. *Sci. Total Environ.* **842**, 156908 (2022).
 41. Wu, R. et al. Molecular composition and volatility of multi-generation products formed from isoprene oxidation by nitrate radical. *Atmos. Chem. Phys.* **21**, 10799–10824 (2021).
 42. Compermolle, S., Ceulemans, K. & Müller, J.-F. Influence of non-ideality on condensation to aerosol. *Atmos. Chem. Phys.* **9**, 1325–1338 (2009).
 43. Bowman, F. M. & Melton, J. A. Effect of activity coefficient models on predictions of secondary organic aerosol partitioning. *J. Aerosol Sci.* **35**, 1415–1438 (2004).
 44. Donahue, N. M., Epstein, S. A., Pandis, S. N. & Robinson, A. L. A two-dimensional volatility basis set: 1. organic-aerosol mixing thermodynamics. *Atmos. Chem. Phys.* **11**, 3303–3318 (2011).
 45. Vione, D., Maurino, V., Minero, C. & Pelizzetti, E. Aqueous atmospheric chemistry: Formation of 2,4-dinitrophenol upon nitration of 2-nitrophenol and 4-nitrophenol in solution. *Environ. Sci. Technol.* **39**, 7921–7931 (2005).
 46. Perraud, V. et al. Nonequilibrium atmospheric secondary organic aerosol formation and growth. *Proc. Natl Acad. Sci. USA* **109**, 2836–2841 (2012).
 47. Peltonen, L. J. & Yliruusi, J. Surface pressure, hysteresis, interfacial tension, and CMC of Four Sorbitan Monoesters at water-air, water-hexane, and hexane-air interfaces. *J. Colloid Interface Sci.* **227**, 1–6 (2000).
 48. González-Dávila, M., Santana-Casiano, J. M. & Pérez-Peña, J. Partitioning of hydrochlorinated pesticides to chitin in seawater: Use of a radial-diffusion model to describe apparent desorption hysteresis. *Chemosphere* **30**, 1477–1487 (1995).
 49. Kenseth, C. M. et al. Particle-phase accretion forms dimer esters in pinene secondary organic aerosol. *Science* **382**, 787–792 (2023).
 50. Berndt, T. et al. Accretion product formation from self- and cross-reactions of RO₂ radicals in the atmosphere. *Angew. Chem. -Int. Ed.* **57**, 3820–3824 (2018).
 51. Peräkylä, O. et al. Large gas-phase source of esters and other accretion products in the atmosphere. *J. Am. Chem. Soc.* **145**, 7780–7790 (2023).
 52. Riva, M., Robinson, E. S., Perraudin, E., Donahue, N. M. & Villenave, E. Photochemical aging of secondary organic aerosols generated from the photooxidation of polycyclic aromatic hydrocarbons in the gas-phase. *Environ. Sci. Technol.* **49**, 5407–5416 (2015).
 53. Ding, A., Wang, T. & Fu, C. Transport characteristics and origins of carbon monoxide and ozone in Hong Kong, South China. *J. Geophys. Res.: Atmos.* **118**, 9475–9488 (2013).
 54. Liu, Y. et al. Aerosol phase state and its link to chemical composition and liquid water content in a subtropical coastal megacity. *Environ. Sci. Technol.* **53**, 5027–5033 (2019).
 55. Shen, M. et al. Release and gas-particle partitioning behavior of liquid crystal monomers during the dismantling of waste liquid crystal display panels in E-waste recycling facilities. *Environ. Sci. Technol.* **56**, 3106–3116 (2022).
 56. Jenkin, M. E., Saunders, S. M., Wagner, V. & Pilling, M. J. Protocol for the development of the Master Chemical Mechanism, MCMv3 (Part B): Tropospheric degradation of aromatic volatile organic compounds. *Atmos. Chem. Phys.* **3**, 181–193 (2003).
 57. Bloss, C. et al. Development of a detailed chemical mechanism (MCMv3.1) for the atmospheric oxidation of aromatic hydrocarbons. *Atmos. Chem. Phys.* **5**, 641–664 (2005).
 58. Xue, L. K. et al. Ground-level ozone in four Chinese cities: precursors, regional transport and heterogeneous processes. *Atmos. Chem. Phys.* **14**, 13175–13188 (2014).
 59. Johnson, D., Jenkin, M. E., Wirtz, K. & Martin-Reviejo, M. Simulating the formation of secondary organic aerosol from the photooxidation of aromatic hydrocarbons. *Environ. Chem.* **2**, 35 (2005).

Acknowledgements

This work was supported by the National Natural Science Foundation of China (42122062), Research Grants Council (RGC) of Hong Kong Special Administrative Region, China (16201623, 16205724, 16209022, T24–504/17–N), and French ANR/RGC Joint Research Scheme (project A–PolyU502/16–SEAM). The authors would like to acknowledge the HKPolyU University Research Facility in Chemical and Environmental Analysis (UCEA) for the equipment support, and Hong Kong Environmental Protection Department and Hong Kong Observatory for providing access to the Cape D’Aguilar Supersite AQMS and for sharing the trace gases, particles and VOCs data at the Supersite. Besides, the authors would appreciate Steven Poon for helping establish the platform of the field campaign to ensure the implementation of the research.

Author contributions

Y.C., M.X. and P.Z. conducted the field campaign with the guidance of Z.W.; Z.Z. and M.X. collected the data of trace gases and J_{NO₂}; Q.Y. and S.L. provided the VOCs data; Z.J.Y. and J.L. provided the OC and EC data; Y.C. and Z.W. did the data analysis; Y.L. performed the regional model analysis; S.T. and K.L. contributed valuable comments to the writing of this paper; Z.W. and T.W. provided the funding sources; Y.C. wrote the original draft, and all the authors participated in the review and editing. All authors read and approved the final manuscript.

Competing interests

The authors declare no competing interests.

Additional information

Supplementary information The online version contains supplementary material available at

<https://doi.org/10.1038/s41612-025-01156-z>.

Correspondence and requests for materials should be addressed to Zhe Wang.

Reprints and permissions information is available at <http://www.nature.com/reprints>

Publisher's note Springer Nature remains neutral with regard to jurisdictional claims in published maps and institutional affiliations.

Open Access This article is licensed under a Creative Commons Attribution-NonCommercial-NoDerivatives 4.0 International License, which permits any non-commercial use, sharing, distribution and reproduction in any medium or format, as long as you give appropriate credit to the original author(s) and the source, provide a link to the Creative Commons licence, and indicate if you modified the licensed material. You do not have permission under this licence to share adapted material derived from this article or parts of it. The images or other third party material in this article are included in the article's Creative Commons licence, unless indicated otherwise in a credit line to the material. If material is not included in the article's Creative Commons licence and your intended use is not permitted by statutory regulation or exceeds the permitted use, you will need to obtain permission directly from the copyright holder. To view a copy of this licence, visit <http://creativecommons.org/licenses/by-nc-nd/4.0/>.

© The Author(s) 2025